Designing Durable Vapor-Deposited Surfaces for Reduced Hydrate Adhesion

Hossein Sojoudi, Matthew R. Walsh, Karen K. Gleason,* and Gareth H. McKinley*

The formation and accumulation of clathrate hydrates inside oil and gas pipelines cause severe problems in deep-sea oil/gas operations. In the present work, durable and mechanically robust bilayer poly-divinyl benzene/poly(perfluorodecylacrylate) coatings are developed using initiated chemical vapor deposition (iCVD) to reduce the adhesion strength of hydrates to underlying substrates (silicon and steel). Tetrahydrofuran (THF) dissolved in water with a wt% concentration of 0–70 is used to study the formation of hydrates and their adhesion strength. Goniometric measurements of the THF–water droplets on the substrates exhibit a reduction in advancing and receding contact angles with an increase in the THF concentration. The strength of hydrate adhesion experiences a tenfold reduction when substrates are coated with these iCVD polymers: from 1050 ± 250 kPa on bare silicon to 128 ± 100 kPa on coated silicon and from 1130 ± 185 kPa on bare steel to 153 ± 86 kPa on coated steel. The impact of subcooling temperature and time on the adhesion strength of hydrate on substrates is also studied. The results of this work suggest that the THF–water mixture repellency of a given substrate can be utilized to assess its hydrate-phobic behavior; hence, it opens a pathway for studying hydrate-phobicity.

1. Introduction

The formation and accumulation of clathrate hydrate deposits inside oil and gas pipelines causes severe problems in deep-sea oil and gas operations.[1,2] Clathrate hydrates are nonstoichiometric crystalline solids formed by physical combinations of water and small gas (e.g., methane, ethane, carbon dioxide, propane) or liquid (e.g., cyclopentane, tetrahydrofuran) guest molecules.[3–5] At the appropriate thermodynamic conditions (in most cases corresponding to relatively high pressures and low temperatures), water as the host molecule forms a framework through a hydrogen bonding network of cages which can be occupied by the guest molecules, whose diameter is less than the size of the cavity.[6]

Active methods have been developed to prevent the formation of hydrate inside oil and gas pipelines by applying heat to the pipelines,[7,8] adding water-miscible alcohols such as methanol to shift the thermodynamic equilibrium away from hydrate formation,[9] and using kinetic inhibitors to delay the crystallization and growth of hydrates.[5,10] However, these methods are expensive, require substantial power for operation, and may have detrimental environmental consequences.[5,7–10] Therefore, surface modification is of great interest for the passive prevention of hydrate formation directly on the surface. Additionally, should any hydrate form, either on the surface or in the bulk, reducing the adhesion strength of the hydrate to the surface is desirable for ease of clearing the blockage.[11] To this end, there is a need for mechanisms enabling deposition of scalable and durable hydrate-phobic coatings which possess required mechanical properties to be applied inside oil and gas pipelines.

In this work, we have developed durable and mechanically robust bilayer polymer coatings using the initiated chemical vapor deposition (iCVD) technique to reduce the adhesion of hydrates to underlying substrates (silicon and steel). iCVD is a deposition technique that enables grafting of polymers to substrates and therefore promotes their adhesion to substrates to be durable against abrasion and erosion.[12–14] Unlike traditional polymer deposition techniques such as spin-coating, dipping, and ink-jet printing, iCVD provides ways to deposit graded polymers, copolymers which do not have common solvents, and multilayered polymers which are covalently bonded at their interface.[15,16] The conformal nature of the iCVD technique also enables the integration of polymer thin films onto engineering surfaces that have roughened features or nanostructured topography. We recently developed bilayer polymers which are covalently bonded to substrates using an in situ grafting mechanism.[17] Such bilayer polymers were shown to exhibit enhanced mechanical properties (e.g., elastic modulus and hardness) when compared to other coatings developed using traditional iCVD polymerization, which potentially makes

Dr. H. Sojoudi, Prof. K. K. Gleason
Department of Chemical Engineering
Massachusetts Institute of Technology
77 Massachusetts Avenue, Cambridge, MA 02139, USA
E-mail: kkg@mit.edu
Dr. H. Sojoudi, Prof. G. H. McKinley
Department of Mechanical Engineering
Massachusetts Institute of Technology
77 Massachusetts Avenue, Cambridge, MA 02139, USA
E-mail: gareth@mit.edu
Dr. M. R. Walsh
Chevron Energy Technology Company
Flow Assurance Technology
1200 Smith St, Houston, TX 77018, USA

ADVANCED
MATERIALS
INTERFACES
www.advmatinterfaces.de

Materials
Views
www.MaterialsViews.com

FULL PAPER

them suitable for industrial applications such as flow assurance strategies by coating inside oil and gas pipelines. Other types of vapor deposition methods have been commercialized for coating the inside of pipes used in the oil and gas industry[18] and it is anticipated that similar process strategies would be successful for iCVD. For applications, including surface modification to improve the release of rubber from the molds used to manufacture tires, the iCVD process has been scaled up to reactors > 1 m in dimension.[12]

Among numerous compounds known to form hydrates with water, tetrahydrofuran (THF) is attractive for laboratory studies since it is in liquid state at atmospheric pressure and is miscible with water, simplifying the experimental procedure and eliminating concerns about intimacy of hydrate/surface contact which would come with formation of a water-immiscible former on a surface; to be sure, the nature of surface contact and adhesion of water-immiscible hydrates is of industrial interest, however, future analogous investigations should concentrate on hydrates of gas and liquid hydrocarbon formers. At atmospheric pressures, hydrates form from THF above the freezing temperature of water (up to 4.4 °C), making them easily distinguishable from ice.[9,19–22] Hydrates are known to crystallize in three common structures, I (sI), II (sII), and H (sH), depending on the size and shape of the guest molecules. THF forms a structure II hydrate with water at a composition of 1:17 molar ratio or ≈19% by weight.[3,23,24] We understand that natural gas is relatively immiscible in water and that the natural gas hydrate formation mechanism inside oil/gas pipelines is governed by the hydrocarbon/water interfacial area and mass/heat transfer. Therefore, the natural gas hydrate formation mechanism is different than fully miscible THF hydrate formation. However, it is not trivial to study the formation and subsequent adhesion of hydrates of water-immiscible formers on surfaces. We believe that a commonly used ambient pressure hydrate former such as THF enables direct formation of hydrates on surface using various hydrate-former concentrations and enables examining the strength of their adhesion on various surfaces; hence, it opens a pathway for studying hydrate-phobicity.

While the crystallization, growth, and aggregation of hydrates have been studied extensively,[5,9,22,25] there are relatively fewer studies focusing on hydrate adhesion to various surfaces. Sloan and co-workers have investigated the formation and adhesion of hydrate particles in a series of studies.[26–28] They used a micromechanical adhesion apparatus to measure adhesion force between already formed hydrate particles,[26,29] and/or hydrate and ice particles with and without the presence of other liquid (e.g., crude oil).[27,28] The effects of contact force, contact time, and subcooling temperature were investigated in these studies.[26–30] Song et al. studied interaction behavior between hydrate particles and water in a temperature-controlled hydrocarbon environment utilizing an apparatus fabricated with a microbalance and z-axis stage.[31,32] Both groups explained the adhesion forces and trends by a capillary bridge forming between the contacting hydrate particles and/or hydrate particles and liquid droplets. More recently, Aspenes et al. studied the adhesion forces between hydrate particles and solid surfaces with various surface energies in the presence of water and/or other petroleum acids in an oil phase.

They found that the adhesion force between the hydrate particles and the solid surfaces increases more than tenfold when the solid surfaces are water-wet.[30] In these studies, hydrate particles were formed by freezing ice particles inside a bath of hydrate-forming liquid and then brought into contact with either similarly formed hydrate particles and/or various solid surfaces. To understand the impact of hydrates crystallization on their adhesion strength, there is a need to study the formation and subsequent adhesion of hydrates on surfaces and investigate the effect of surface energy on their adhesion strength.

Here, we study both the formation and subsequent adhesion of THF hydrates on surfaces coated with iCVD polymers. The composition of THF in water was varied and its impact on the surface tension of the THF–water mixture and contact angle of the THF–water droplets on polymer-coated surfaces has been studied. By understanding the phase diagram of the THF–water mixture, the number of experimental measurements required to predict the behavior of a surface at all THF compositions can be minimized. Additionally, our work demonstrates the optimal THF compositions to work with in order to predict the behavior of hydrates over the full range of compositions.

Recently, we reported the deposition and process optimization of iCVD bilayer polymers with enhanced mechanical properties and adhesion to substrates as well as their hydrophobicity/icephobicity.[17] The bilayer polymers consisted of a thick, mechanically robust, and dense polymer base layer, poly-divinyl benzene (pDVB), that is highly crosslinked and then capped with a covalently attached thin fluorine-containing top layer, poly(perfluorodecylacrylate) (pPFDA). A linker-free grafting in which covalent chemical bonds form across the substrate–polymer interface was developed to enhance the interfacial adhesion of the bilayer iCVD polymers to the underlying substrates. With this bilayer architecture, the optimized film displayed both high elastic modulus, E, and hardness, H ($E = 19.1 \pm 1.2$ GPa and $H = 479.0 \pm 7.0$ MPa) and excellent Cassie-state hydrophobicity (advancing water contact angle (WCA), $\theta_A = 157.8° \pm 2.3°$, and receding WCA, $\theta_R = 131.0° \pm 8.0°$). In addition, the linker-free grafted bilayer films did not delaminate during nanoscratch tests performed at 5 mN normal loads.[17] Finally, the strength of ice adhesion was reduced by more than sixfold when substrates were coated with these bilayer films as a result of the low surface energy and smoothness of the iCVD coatings.

In the present work, these optimized linker-free grafted iCVD bilayer films are extended into a new area of durable hydrate-phobic surfaces. This important application can leverage what is known about the popular topics of hydrophobic and icephobic surfaces. As discussed earlier, THF is used as a hydrate former due to its unlimited solubility in water and ease of hydrate formation. For various concentrations of THF dissolved in water, the formation of hydrates and the subsequent strength of their adhesion on bilayer iCVD polymers are studied. The results of this study indicate that simple measurements of contact angles and surface tension of THF–water droplets on substrates are a powerful tool to evaluate the adhesion strength of hydrates to such substrates; hence, it can be used as a key parameter for design of hydrate-phobic surfaces.

www.MaterialsViews.com

ADVANCED
MATERIALS
INTERFACES
www.advmatinterfaces.de

FULL PAPER

2. Results and Discussion

Deposition and linker-free grafting mechanism of bilayer CVD polymers were extensively explained in our previous work. Thus, only a summary is presented here. First, the growth substrates were cleaned by treatment with solvents (e.g., acetone and methanol) and then exposed to an oxygen plasma to enhance the surface concentration of hydroxyl species. Then, the substrates were placed in a low pressure iCVD reactor. The subsequent grafting and synthesis proceed in three steps, all performed sequentially in the iCVD chamber without breaking vacuum: 1) in situ linker-free grafting, 2) deposition of a mechanically robust crosslinked hydrocarbon network, and 3) deposition of the top fluoropolymer layer.

For the linker-free grafting, tert-butyl peroxide (TBPO) vapors as initiators were exposed to filament arrays kept at $T_f = 310\ °C$ to produce methyl radicals[33,34] which can abstract hydrogen from the hydroxyl groups on the substrate (which is maintained at $T_s = 20\ °C$) and result in activated radical sites on the surface.[33] These sites will directly react with the vinyl monomers which are introduced next, to produce covalent bonds from the substrate to the organic layer.

Next, divinylbenzene (DVB) monomer was introduced to the reactor without filament heating ($T_f = 25\ °C$) while the substrate was kept at $T_s = 20\ °C$. The initial reaction with the activated surface sites results in direct grafting of the monomer to the substrate while retaining a free electron for subsequent vinyl polymerization.

For polymerization of the mechanically robust layer in the second step, DVB, N_2, and TBPO were introduced simultaneously to the low pressure reactor while the filament and the substrate were kept at $T_f = 250\ °C$ and $T_s = 30\ °C$, respectively.[35] This resulted in deposition of a densely crosslinked DVB polymer (pDVB) network with the desired thickness (in the range of 200 nm–1 μm).

The third and final step is to grow a top surface layer displaying both low surface energy and the desired hydrate-phobicity. For this, poly-perfluorodecylacrylate, poly-(1H, 1H, 2H, 2H-perfluorodecylacrylate) (pPFDA) was introduced to deposit a thin layer of fluorine-rich polymer (either 10 or 40 nm thick). It has been shown that the presence of the densely crosslinked pDVB network underneath a thin pPFDA film can prevent inward reorientation of fluorine groups in pPFDA film when exposed to water and results in a lower WCA hysteresis.[16] Therefore, around 10 nm of pPFDA on crosslinked pDVB is favorable to obtain a bilayer film (abbreviated as LFG-BL (10 nm)) with very low WCA hysteresis (3.8° ± 0.5°). On the other hand, a relatively thicker layer of pPFDA (≈40 nm) grafted to the underlying pDVB was believed to have slightly higher fluorine concentration (abbreviated as LFG-BL (40 nm)) resulting in higher values of the advancing WCA (157.8° ± 2.3°) and relatively high receding WCA (131.0° ± 8.0°). Therefore, two sets of bilayer films (LFG-BL (10 nm) and LFG-BL (40 nm)) were developed in this work to investigate the impact of both contact angle and contact angle hysteresis on the subsequent adhesion of THF/water hydrate deposits.

Fourier transform infrared spectroscopy (FTIR) was performed on the bilayer polymer and confirmed successful deposition of both pPFDA and pDVB components through the presence of bands corresponding to carbonyl, carbon–fluorine bonds, and phenyl groups in the FTIR spectra.[17] The properties of the LFG-BL films can be summarized as follows. Optical profilometer measurement gave root mean square (R_q) roughness values of 18.9 ± 5.4 and 19.2 ± 4.8 nm for LFG-BL (40 nm) and LFG-BL (10 nm) coatings, respectively.[17] Elastic modulus and hardness were obtained from nanoindentation measurements and found to be $E = 19.1 ± 1.2$ GPa and $H = 479.0 ± 7.0$ MPa for LFG-BL (40 nm) and $E = 18.1 ± 1.0$ GPa and $H = 463.0 ± 4.5$ MPa for LFG-BL (10 nm). It is important to note that the elastic modulus and hardness mostly depend on the highly crosslinked pDVB network and not on the properties of the thin top layer pPFDA film; therefore, LFG-BL (40 nm) and LFG-BL (10 nm) showed comparable elastic modulus and hardness values.

2.1. THF–Water Wettability of Surfaces

Water is an extensively hydrogen-bonded fluid and the addition of cyclic ethers such as tetrahydrofuran leads to the formation of clathrates with the ether molecules being surrounded by water molecules.[36] Solutions of THF–water mixture (0, 10, 19, 50, and 70 wt% THF in water or

$$\chi_{THF} = \frac{\text{wt. THF}}{\text{Total wt.}} = 0, 0.1, 0.19, 0.50, \text{ and } 0.70) \text{ were made and}$$

their surface tension and their impact on wettability of surfaces (iCVD polymer coated and bare substrates) were studied. The surface tension values of the THF–water mixtures were measured through the pendant drop method.[37] Measurements were performed rapidly (less than 10 s) to minimize impact of air exposure on the THF–water droplets. The surface tension values were averaged from measurements of ten droplets for a given composition of THF in water. Variation of the surface tension with wt% of THF dissolved in water is illustrated in Figure S1, Supporting Information. The measured surface tension of DI water was within the acceptable range, 70.5 ± 1.5 mN m^{-1}, and used for verification of surface tension data for other THF–water mixtures. As expected, the surface tension of the THF–water mixture decreases with an increase in the wt% of THF in water.[36]

The wettability of bare and iCVD polymer-coated substrates also displayed a dependence on the wt% of THF in water. The wettability of a surface by a liquid can be enhanced by either reducing the liquid surface tension or increasing substrate surface energy. Contact angle measurements are a useful tool for probing interfacial interactions between solid and liquid. Wettability of a solid surface is characterized by the contact angle measured between the liquid drop and the surface. In a typical solid–liquid–vapor system (such as a sessile drop of liquid placed on a solid surrounded by air), the contact angle can also be used to measure the work of adhesion.[38] Wetting of a surface by a particular liquid depends on the relative magnitude of the cohesive molecular forces that exist within the liquid and adhesive interaction between liquid and the solid. Strong adhesive forces between a liquid and solid result in a liquid drop spreading across the surface. Strong cohesive forces within the liquid prevent contact with the surface. Strong adhesion and weak cohesion result in a high degree of wetting, a hydrophilic condition with low measured contact angles. Conversely, weak
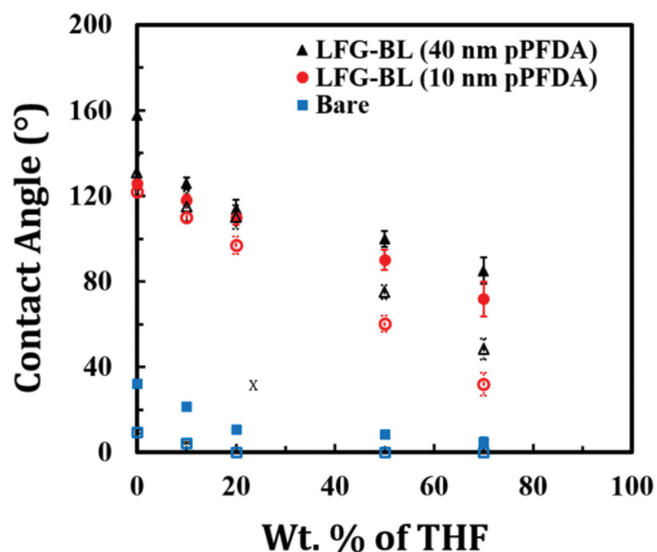
Figure 1. THF–water mixture advancing and receding contact angle on bare, linker-free grafted bilayer pDVB/pPFDA with an ≈40-nm-thick pPFDA (LFG-BL (40 nm)), and linker-free grafted bilayer pDVB/pPFDA with an ≈10-nm-thick pPFDA (LFG-BL (10 nm)) substrates. Both advancing, θ_A (filled symbols), and receding, θ_R (hollow symbols) contact angles decrease due to the reduction in the surface tension of the THF–water mixture as wt% of the THF in the mixture increases ($0 \leq \chi_{THF} \leq 0.70$).

adhesion and strong cohesion result in hydrophobic conditions with high measured contact angles and poor wetting.[39–41]

Figure 1 shows advancing and receding contact angles of THF–water mixture droplets on coated and bare substrates. It is evident that with an increase in the wt% of THF in the mixture (higher χ_{THF}) both the advancing and receding contact angles of the THF–water droplets on all of the substrates decrease because of the adhesive interaction between the substrate and the liquid. Linker-free grafted bilayer pDVB/pPFDA polymer with ≈40-nm-thick pPFDA (LFG-BL (40 nm)) presents both a high advancing (157.8° ± 2.3°) and high receding (131.0° ± 8.0°) water contact angle. Addition of 70 wt% THF in water ($\chi_{THF} = 0.70$) results in lower advancing (85.1° ± 6.1°) and receding (48.5° ± 4.9°) THF–water contact angles on LFG-BL (40 nm). However, the coating does not become fully wetted due to the high density of fluorine-containing groups on the coatings. In contrast, bare substrates become wet spontaneously with the THF–water mixture.

The goniometer measurements on linker-free grafted bilayer pDVB/pPFDA with a smaller pPFDA top coat thickness of ≈10 nm (LFG-BL (10 nm)) resulted in advancing and receding water contact angles of 125.8° ± 1.1° and 122.0° ± 2.0°, respectively. Droplets of 70 wt% THF in water solution ($\chi_{THF} = 0.70$) exhibited advancing and receding contact angle of 71.8° ± 8.2° and 32.0° ± 5.3° on these samples, respectively. The reduction in the average advancing and receding contact angles on LFG-BL (10 nm) when compared to LFG-BL (40 nm) might be due to slightly reduced fluorine concentration or differences in the crystallinity of the PFDA layer in the bilayer film.[13] X-ray photoelectron spectroscopy was performed and confirmed the presence of fluorine groups in the bilayer films. The survey spectra showed the most prominent peaks to be C1s, O1s, and F1s (Figure S2, Supporting Information).[42–44] High resolution XPS

spectra of F1s and C1s binding energy (BE) were also acquired. The fluorine to carbon ratio in the LFG-BL (40 nm) is slightly higher when compared to LFG-BL (10 nm): 56.7% fluorine and 38.3% carbon in LFG-BL (40 nm) whereas the ratio drops to 55.6% fluorine and 39.3% carbon in LFG-BL (10 nm) (Table S1, Supporting Information). However, for photoelectrons generated by Al Kα excitation with a take-off angle (TOA) of 45°, 10 nm is about the maximum escape depth expected. One can argue that the slight difference in the fluorine to carbon concentration between the nominally 10- and 40-nm-thick pPFDA top layers could be an effect of the penetration depth. In the LFG-BL (10 nm), the XPS may sample the entire pPFDA layer and then possibly goes deeper into the underlying pDVB whereas in the LFG-BL (40 nm), most likely only the top layer (pPFDA) is sampled. Another possible explanation for the different THF–water repellency nature of the thin (10 nm) and the thick (40 nm) bilayer films could be due to the differences in their crystallinity.[15] A slight decrease in contact angle hysteresis (advancing contact angle minus receding contact angle) was also observed. Overall, the thicker LFG-BL (40 nm) coating shows better THF–water mixture repelling nature when compared to the thinner LFG-BL (10 nm) and suggests that the former coating is likely to perform better for reduction of THF hydrate adhesion strength.

2.2. THF Hydrate Formation and Strength of Adhesion to Surfaces

We next study the formation and accumulation of THF hydrates on coated surfaces with a systematic variation in surface energies. Natural gas hydrates usually form at elevated pressures due to their low solubility in water. Mass transfer at the liquid–gas interface controls nucleation and crystal growth of these hydrates.[9,10,45] THF–water hydrate is often used as a model miscible system for the study of hydrate formation because interfacial mass transfer effects are eliminated, and because the necessity of high pressure is also eliminated.[9] The THF–water phase diagram is a useful tool to study the formation of THF hydrates (Figure S3 Supporting Information). THF is miscible in water and forms a structure II hydrate with water at a composition of 1:17 molar ratio (≈19 wt% THF dissolved in water, $\chi_{THF} = 0.19$). This hydrate melts at a temperature of 4.4 °C (277.4 K) at 1 atm.[3] According to the phase diagram, when the concentration of THF in water is less than ≈19 wt% ($\chi_{THF} < 0.19$), the THF–water mixture converts to a mixture of ice and hydrates when cooled down to low temperature (≤271.0 K) at atmospheric pressure (denoted regime I). On the other hand, a THF–water mixture with more than ≈19 wt% THF ($\chi_{THF} > 0.19$) will partially convert to hydrates with some unfrozen THF-rich supernatant solution when cooled to a low temperature (denoted regime II).[3]

Here, we study the formation of hydrates and/or ice and the strength of their adhesion to bare and polymer-coated substrates in both regimes. A custom-built adhesion testing apparatus housed inside a nitrogen-containing glove box was used for this purpose.[46] Various wt% of THF dissolved in water ($\chi_{THF} = 0$, 0.10, and 0.19 in regime I and $\chi_{THF} = 0.19$, 0.50, and 0.70 in regime II) were prepared and poured into glass cuvettes and were frozen on test substrates (bare and polymer-coated surfaces)

Table 1. Values measured for the strength of ice, ice/hydrate, and hydrate/unfrozen liquid on bare, linker-free grafted bilayer pDVB/PPFDA with an ≈10 nm pPFDA (LFG-BL (10 nm)), and linker-free grafted bilayer pDVB/PPFDA with an ≈40 nm pPFDA (LFG-BL (40 nm)) coated substrates. In regime I ($0 \leq \chi_{THF} \leq 0.19$), an increase in the amount of hydrate in the solid results in a decrease in the strength of solid (ice/hydrate) adhesion. In regime II ($\chi_{THF} \geq 0.19$), increasing the wt% of THF does not change the stoichiometric composition of the hydrate that forms but increases the amount of unfrozen liquid. This reduces the total strength of adhesion against each substrate (bare and coated silicon).

Sample	$\chi_{THF} = 0$ ice [kPa]	$\chi_{THF} = 0.10$ ice+hydrate [kPa]	$\chi_{THF} = 0.19$ hydrate [kPa]	$\chi_{THF} = 0.50$ hydrate+unfrozen liquid [kPa]	$\chi_{THF} = 0.70$ hydrate+unfrozen liquid [kPa]
Bare	1127 ± 250	1100 ± 100	1050 ± 250	850 ± 220	267 ± 102
LFG-BL (10 nm)	473 ± 185	390 ± 60	320 ± 84	230 ± 100	92 ± 60
LFG-BL (40 nm)	250 ± 115	185 ± 75	128 ± 250	80 ± 31	40 ± 15

for several hours at −15 °C to ensure formation of hydrates and/or ice on each substrate.[11] In order to prevent THF evaporation, care was taken to minimize air exposure of the THF–water mixture, and the time elapsed between its preparation and pouring into cuvettes for strength of adhesion measurements.

The lateral force required to de-adhere frozen cuvettes was recorded and converted into a measure of the shear strength of ice/hydrate adhesion by dividing over the cuvette area. The measurements were performed on 20 samples of each type and subsequently averaged. Sample-to-sample variations in the measured adhesion strengths can be large due to the dominant role of local flaws in this failure test and variations in the nature of the ice/hydrate formed at the interface with the substrate.

2.2.1. Regime I: $0 \leq \chi_{THF} \leq 0.19$

At a composition of 19 wt% THF in water the mixture turns fully into hydrates when cooled down to low temperature at atmospheric pressure.[5,26,36,45] The strength of the hydrate adhesion measured on bare silicon substrates was 1050 ± 250 kPa, whereas the corresponding value on LFG-BL (10 nm) and LFG-BL (40 nm) coated silicon substrates were measured to be 320 ± 84 and 128 ± 250 kPa, respectively. This indicates that the polymer coating with the LFG-BL (40 nm) resulted in an approximately tenfold reduction in the strength of hydrate adhesion when compared to bare silicon substrates. The reduction in adhesion by LFG-BL (40 nm) was found to be superior to that of LFG-BL (10 nm), consistent with the better THF–water repelling nature of the LFG-BL (40 nm) as shown in Figure 1. At compositions of $\chi_{THF} < 0.19$ cooling to low temperatures results in formation of both ice and hydrate. Based on the THF–water phase diagram using the lever rule,[3] a composition of $\chi_{THF} \cong 0.10$ water turns into ≈50% ice and ≈50% hydrates when cooled to low temperatures. At this concentration of THF, the strength of the ice/hydrate mixture adhesion on bare silicon substrates was measured to be 1100 ± 100 kPa, whereas on LFG-BL (10 nm) and LFG-BL (40 nm) the values were 390 ± 60 and 185 ± 75 kPa, respectively. Again we find that the fluorinated polymer bilayer coating resulted in substantially lowered adhesion strength of ice/hydrate mixture (close to tenfold reduction).

Comparing adhesion strength of ice/hydrate mixture with that of pure hydrate on a given substrate indicates that the addition of ice results in enhanced adhesion strength of the solid (ice and/or hydrate) to both bare and coated silicon substrates. Finally, the cuvettes were filled with only water and the adhesion of pure ice was measured on the bare and polymer-coated silicon

substrates. The strength of ice adhesion was 1127 ± 250 kPa on bare silicon substrates and 473 ± 185 and 250 ± 115 kPa on the LFG-BL (10 nm) and the LFG-BL (40 nm) coated silicon substrates, respectively. These values are summarized in **Table 1**.

Figure 2a shows the measured strength of solid (ice and/or hydrate) adhesion plotted versus the amount of hydrate in solid ($0 \leq w \leq 1$), which can be related to χ_{THF} (0–0.19) using the THF–water phase diagram.[3] A linear fit to the adhesion strength data for a given substrate (bare silicon or polymer-coated silicon) leads to a relation that enables us to express the adhesion strength of ice/hydrate mixture as a function of the individual values of ice adhesion strength and hydrate adhesion strength
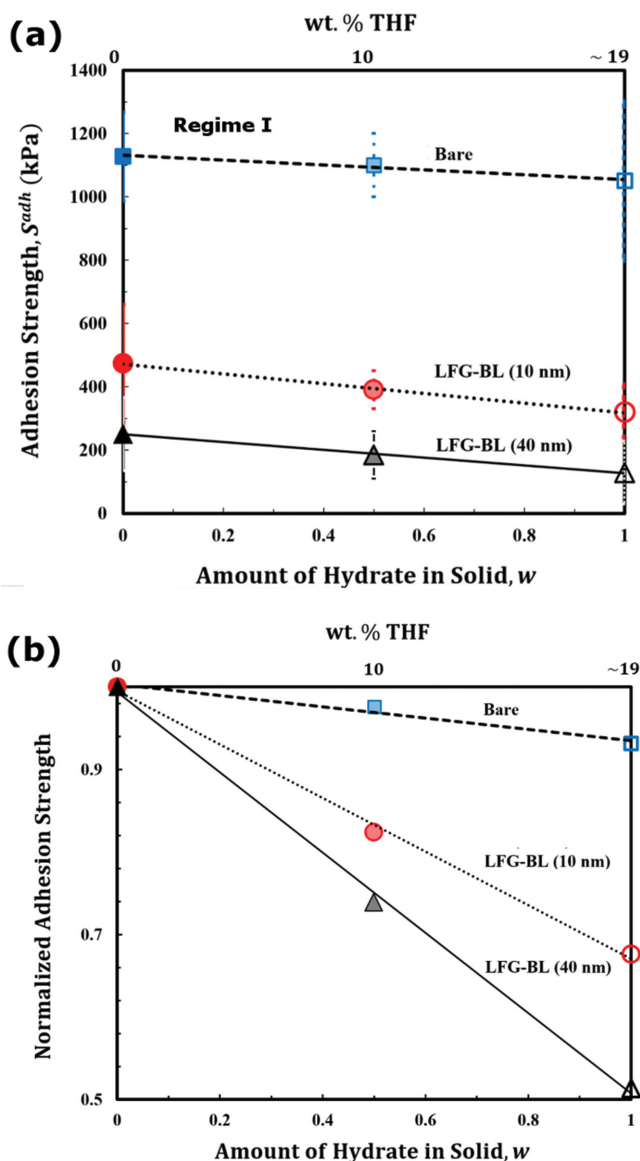
$$S^{adh} = \left[(1-w) \times S_{ice}^{adh} + w \times S_{hydrate}^{adh} \right] \qquad (1)$$

where S^{adh} is the measured strength of crystal solid (ice/hydrate mixture) adhesion, S_{ice}^{adh} is the strength of ice adhesion, and $S_{hydrate}^{adh}$ is the strength of hydrate adhesion. The linear fits through the data show excellent correlation and confirm the validity of the proposed linear relation ($R_{bare}^2 = 0.97$, $R_{LFG-BL(10\,nm)}^2 = 0.99$, and $R_{LFG-BL(40\,nm)}^2 = 0.99$).

This relation can be useful to obtain the adhesion strength of solid crystals formed from THF/water compositions with $0 < \chi_{THF} < 0.19$ on substrates with given surface energy. The average values of the measured adhesion strength of hydrate and/or ice/hydrate mixture were also normalized using the average values of the pure ice adhesion strength measured for a given substrate, as shown in Figure 2b. The results indicate that the ratio of hydrate adhesion strength to ice adhesion strength is reduced from ≈0.93 on bare silicon substrates to ≈0.67 and ≈0.51 on LFG-BL (10 nm) and LFG-BL (40 nm) coated silicon substrates, respectively. This indicates that the reduction in the adhesion strength of THF hydrate when compared to adhesion strength of ice is enhanced on surfaces with higher fluorine concentration. Similarly, through a linear fit to the normalized adhesion strength data, the normalized strength of crystal solid (ice/hydrate mixture) adhesion, $S^{adh-norm}$, can be obtained using w and the normalized strength of hydrate adhesion, $S_{hydrate}^{adh-norm}$. The values obtained from these linear fits for S_{ice}^{adh}, $S_{hydrate}^{adh}$, and $S^{adh-norm}$ are presented in **Table 2** for bare, LFG-BL (10 nm), and LFG-BL (40 nm) coated silicon substrates.

2.2.2. Regime II: $\chi_{THF} \geq 0.19$

When the concentration of THF in water exceeds 19 wt%, upon freezing the THF–water mixture will partially convert

ADVANCED
MATERIALS
INTERFACES
www.advmatinterfaces.de

Materials Views
www.MaterialsViews.com

Table 2. Values obtained from linear regression of the measured values for the strength of ice adhesion, S_{ice}^{adh}, the strength of hydrate adhesion, $S_{hydrate}^{adh}$, and the normalized hydrate adhesion strength, $S^{adh\text{-}norm}$ for bare, linker-free grafted bilayer pDVB/PPFDA with an ≈10 nm pPFDA (LFG-BL (10 nm)), and linker-free grafted bilayer pDVB/PPFDA with an ≈40 nm pPFDA (LFG-BL (40 nm)) coated silicon substrates.

Sample	Strength of ice adhesion	Strength of hydrate adhesion	Normalized strength of hydrate adhesion
Bare	1131	1053	0.93
LFG-BL (10 nm)	471	317	0.69
LFG-BL (40 nm)	249	128	0.50

is −108.5 °C at 1 atm). Mixtures of 50 and 70 wt% THF in water ($\chi_{THF} = 0.50$ and 0.70) were prepared and poured into cuvettes for adhesion strength tests similar to the protocols explained earlier. Similar to the measurements performed in regime I, the strength of adhesion of the hydrate/unfrozen liquid samples to 20 samples of various bare and coated silicon substrates were obtained to minimize statistical variations.

Figure 3 shows the adhesion strength values versus the amount of liquid converted to hydrates, $0 \leq h \leq 1$. The amount of hydrate formed from a THF–water mixture was calculated from the THF–water phase diagram using the lever rule. For a composition of 50 wt% THF in water ($\chi_{THF} = 0.50$) ≈61% of the liquid turns into hydrate ($h \cong 0.61$). At this THF concentration,

Figure 2. Adhesion strength a) and normalized adhesion strength b) of the ice/hydrates on linker-free grafted bilayer pDVB/pPFDA with an ≈40-nm-thick pPFDA (LFG-BL (40 nm)), linker-free grafted bilayer pDVB/pPFDA with an ≈10-nm-thick pPFDA (LFG-BL (10 nm)), and bare silicon substrates. Hydrates have lower adhesion strength when compared to ice on all silicon substrates. The adhesion strength of ice/hydrates mixture can be expressed as a function of the ice adhesion strength and the hydrate adhesion strength. This relation is useful in predicting the adhesion strength when composition of THF $\chi_{THF} \leq 0.19$ dissolved in water freezes on a given substrate (Regime I).
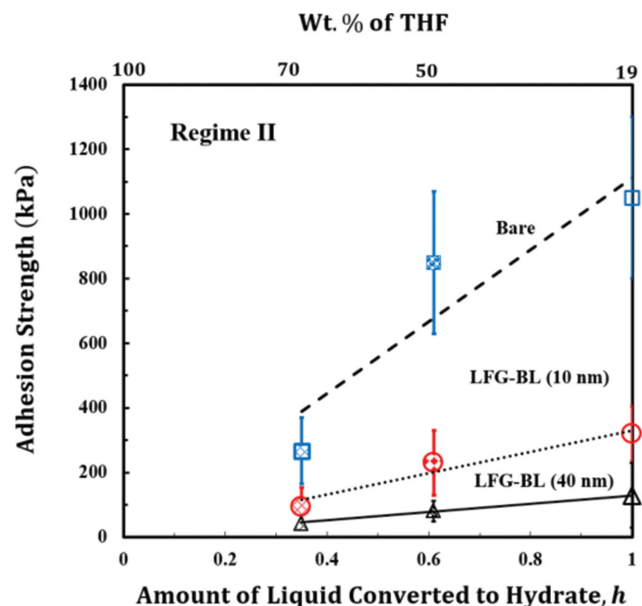
to hydrates at low temperature (−15 °C) with some residual unfrozen liquid. The composition of this supernatant unfrozen liquid depends on the THF wt% in the mixture. The temperature was reduced to as low as −20 °C and maintained for ≈4 h but the amount of unfrozen liquid observable with the naked eye did not change. This is in accord with the THF–water phase diagram[3] which suggests presence of two phases (hydrate and unfrozen supernatant liquid) at these temperatures at atmospheric pressure (the freezing point of pure THF

Figure 3. Adhesion strength of hydrates/unfrozen THF–water mixture on linker-free grafted bilayer pDVB/pPFDA with an ≈40-nm-thick pPFDA (LFG-BL (40 nm)), linker-free grafted bilayer pDVB/pPFDA with an ≈10-nm-thick pPFDA (LFG-BL (10 nm)), and bare silicon substrates. When the composition of THF in water is $\chi_{THF} \geq 0.19$, the THF–water mixture partially freezes to form hydrates (regime II). The composition of unfrozen supernatant THF–water mixture can be estimated from the THF–water phase diagram using the lever rule. A linear fit through the hydrate adhesion strength and the hydrate/unfrozen liquid adhesion strength passes close to origin in the plot. This suggests an overall uniform distribution of hydrates and unfrozen liquid within the cuvettes during the adhesion measurements.

the strength of hydrate/unfrozen liquid adhesion on bare silicon substrates was measured to be 850 ± 220 kPa, whereas on LFG-BL (10 nm) and LFG-BL (40 nm) coated silicon substrates the strength of adhesion was reduced to 230 ± 100 and 80 ± 31 kPa, respectively. An increase in the wt% of THF in water to $\chi_{THF} = 0.70$ results in ≈35% hydrate formation (h ≅ 0.35). As expected this leads to a decrease in the adhesion strength of hydrate/unfrozen liquid on all substrates from 267 ± 102 kPa on bare silicon to 92 ± 60 kPa on the LFG-BL (10 nm), and 40 ± 15 kPa on LFG-BL (40 nm) coatings on silicon substrates. These values are summarized in Table 1.

Linear regression of the hydrates/unfrozen liquid adhesion strength data plotted versus the amount of liquid converted to hydrates, h, approximately passes through the origin with the following relation

$$S^{adh}_{hydrate/unfrozen\ liquid} = h \times S^{adh}_{hydrate} \qquad (2)$$

where $S^{adh}_{hydrate/unfrozen\ liquid}$ is the adhesion strength of the hydrate/unfrozen liquid mixture which forms when the THF wt% in water is $\chi_{THF} > 0.19$ and h is the fraction of the liquid that is converted to hydrates.

It has been shown that hydrophobic hydrate formers allow hydrate crystals to form predominately at the interface of the guest–water phase, whereas the miscibility of THF and water enables hydrate crystals to form and grow anywhere within the confines of the solution.[5,9,45] The linear relation between the adhesion strength and h confirms an overall uniform distribution of hydrates and unfrozen THF–water mixture within the cuvettes during the adhesion measurements. For a given THF wt% in water on a given substrate (χ_{THF}), h can be obtained from the THF–water phase diagram, and the strength of the hydrate that forms from that liquid below a critical temperature can be obtained from the above relation. In addition, it can be concluded that the compositions of the hydrates and the strength of their adhesion to various substrates (bare and polymer-coated) are comparable and independent of the wt% of THF in water that form those hydrates at low temperature.

2.3. Relation between Surface Wettability and the Strength of Ice/Hydrate Adhesion

As explained earlier, when $0 \leq \chi_{THF} \leq 0.19$ freezing results in formation of both hydrate and ice (indicated as regime I) whereas for $\chi_{THF} \geq 0.19$ it causes the formation of hydrate with some residual unfrozen liquid (denoted regime II). **Figure 4**a shows the adhesion strength of ice/hydrate (in regime I) and Figure 4b hydrate/unfrozen liquid (in regime II) plotted versus the advancing contact angle of the liquid THF–water mixture, θ_A, on both coated (LFG-BL (40 nm) and LFG-BL (10 nm)) and bare silicon substrates. The average strength of ice/hydrate adhesion (in regime I) and hydrate/unfrozen liquid adhesion (in regime II) reduces linearly as the advancing contact angle of THF–water mixture increases due to improved wettability of surfaces.

It has been argued that the wettability and motion of liquid droplets on surfaces involve both shear and tensile contributions.[39–41] While the shear contribution is related to sliding and/or roll-off of liquid droplets from surfaces, the tensile force
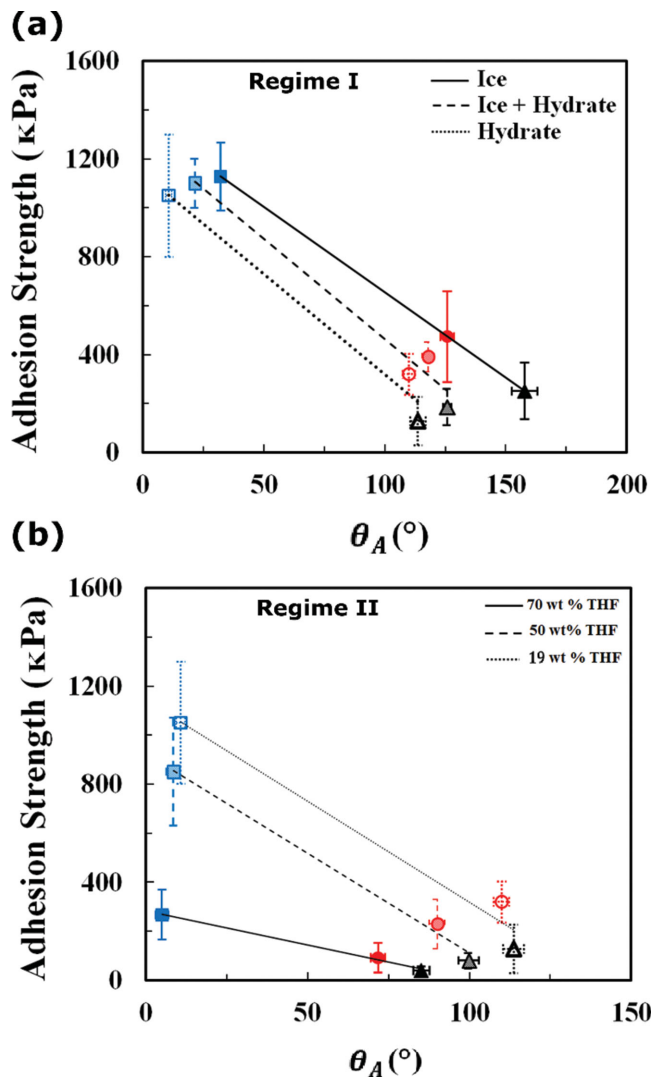
Figure 4. Adhesion strength of ice/hydrate in regime I a) and hydrate/unfrozen liquid in regime II b) versus advancing contact angle, θ_A, of THF–water droplets on linker-free grafted bilayer pDVB/pPFDA with an ≈40-nm-thick pPFDA (LFG-BL (40 nm): black symbols), linker-free grafted bilayer pDVB/pPFDA with an ≈10-nm-thick pPFDA (LFG-BL (10 nm): red symbols), and bare silicon substrates (blue symbols). Composition of THF in water $0 \leq \chi_{THF} < 0.19$ causes formation of both hydrates and ice as indicated by regime I in a), whereas composition of THF in water $\chi_{THF} > 0.19$ results in formation of hydrates with some unfrozen liquid represented as regime II in b). $\chi_{THF} = 0.19$ results in formation of only hydrates as indicated in both regimes. Polymer coatings reduce the wettability of surfaces by THF–water mixture (increase in θ_A) and therefore lower the adhesion strength of ice/hydrate in regime I and hydrate/unfrozen liquid in regime II.

required to detach a liquid droplet from a solid surface depends on the receding contact angle.[46] This is related to the work of adhesion between a liquid droplet (e.g., the THF–water mixture of interest in this study) and the underlying substrate, and can be calculated from the Young–Dupré equation[39–41]

$$W^{adh} = \gamma_{LV}(1 + \cos\theta_R) \qquad (3)$$

ADVANCED
MATERIALS
INTERFACES
www.advmatinterfaces.de

Materials
Views
www.MaterialsViews.com

where W^{adh} is the work of adhesion between a liquid droplet (e.g., the THF–water mixture) and the underlying substrate; γ_{LV} is the surface tension between liquid (e.g., THF–water mixture) and air; and θ_R is the receding contact angle of THF–water liquid droplets on a substrate.

A high receding contact angle for a drop of THF–water mixture on a substrate, θ_R, corresponds to low pull-off forces under tensile (normal) loading conditions. To reflect the importance of this "tensile hydrophobicity," we present the strength of ice/hydrate adhesion data by plotting them versus the work of adhesion between a liquid droplet (e.g., THF–water mixture) and a given substrate (bare and polymer coated) (Figure S4a,b, Supporting Information). For $0 \leq \chi_{THF} \leq 0.19$ (regime I), the ice/hydrate adhesion strength was plotted versus the work of adhesion between a liquid droplet, which was used for the formation of ice/hydrate, and underlying substrate. The average strength of ice/hydrate adhesion linearly reduces with decreases in the work of adhesion (calculated from Equation (3)). This linear reduction suggests that the adhesion strength of the solid ice/hydrate correlates well with the work of adhesion between a liquid THF–water droplet (used to form the ice/hydrate) and the underlying substrate in this regime.

In regime II, $\chi_{THF} \geq 0.19$, the adhesion strength of the hydrate/unfrozen supernatant liquid was plotted versus the work of adhesion between a droplet containing ≈19 wt% THF in water and the underlying substrate (Figure S4b, Supporting Information). These data suggest that liquid drops with a composition of 19 wt% THF in water ($\chi_{THF} = 0.19$) have to be used as a probe fluid to obtain the correct work of adhesion relevant to the strength of hydrates/unfrozen liquid adhesion on substrates.

Overall, good correlation between the measured hydrophobicity of THF–water droplets placed on the deposited polymer films and their measured hydrate-phobic behavior is observed. These results confirm that smooth fluoropolymer surfaces with both high advancing and receding contact angles for liquid THF–water mixtures are optimal for reducing the strength of ice/THF hydrate adhesion. The reduction in the strength of THF hydrate adhesion reported in this work is higher than those values reported elsewhere for soft fluorinated polymer coatings.[46,47] Furthermore, the high modulus and stiffness of the crosslinked polymer networks that are deposited by the iCVD process provide greatly enhanced mechanical resistance to wear and erosion processes that are characteristic of industrial applications.

2.4. Subcooling Effect

The combination of subcooling temperature and time is also important in the formation of THF hydrates. When previously formed hydrate particles are brought into contact with
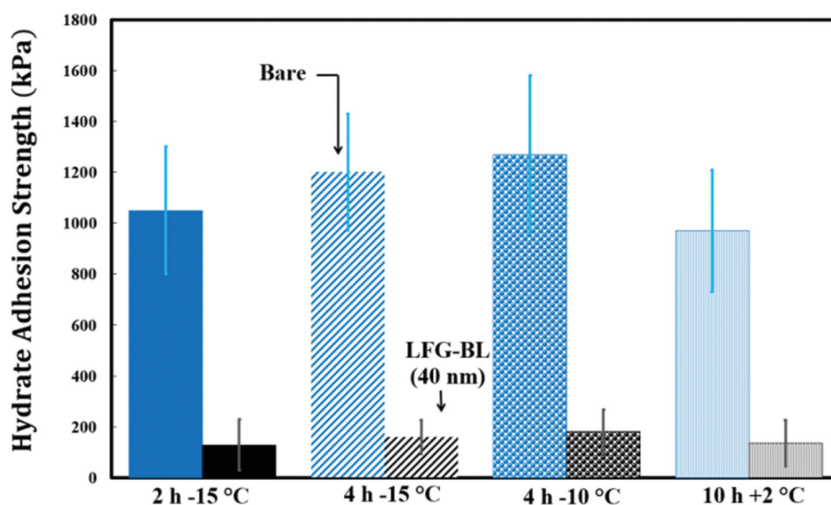
Figure 5. Effects of subcooling temperature and time on the adhesion strength of hydrates formed on coated and bare silicon substrates from a THF–water mixture with $\chi_{THF} = 0.19$. Adhesion strength of hydrates formed on bare and linker-free grafted bilayer pDVB/pPFDA with an ≈40-nm-thick pPFDA (LFG-BL (40 nm)) coated silicon substrates under different subcooling time and temperature. Once the hydrates form, their adhesion strengths are comparable regardless of their formation conditions. Slight difference in the adhesion strength can be attributed to the possible differences in the nucleation and growth of the hydrates. To ensure the presence of only THF hydrates, the samples were allowed to solidify and anneal above the melting point of ice (+2 °C) for a period of 10 h.

each other and/or with a desired test substrate, subcooling plays an important role in the adhesion strength that develops between two interacting parts.[26–28,30] It has been shown that the growth rate of hydrates increases as subcooling temperature and/or time increases.[19,45] To investigate the impact of subcooling temperature and time on the hydrate adhesion strength, a solution with $\chi_{THF} = 0.19$ was prepared and used to study formation of THF hydrates on bare and polymer-coated silicon substrates (LFG-BL (40 nm)) under various solidification conditions.

Figure 5 shows the adhesion strength of the hydrate formed under different subcooling temperatures and time on bare and LFG-BL (40 nm) coated silicon substrates. Neither the increase in cooling time from 2 to 4 h nor the increase in the cooling temperature from −15 to −10 °C caused a noticeable change in the hydrate adhesion strength. To ensure the presence of only hydrates, they were intentionally allowed to nucleate above the melting point of ice (+2 °C) for a period of 10 h. The measurements were performed on bare and LFG-BL (40 nm) coated silicon substrates and hydrate adhesion strength comparable to the previous values presented above in Section 2.2.1 were obtained. The hydrate adhesion strength values on LFG-BL (40 nm) coated substrates normalized by the hydrate adhesion strength on bare substrates (Figure S5, Supporting Information). When represented in this form it shows that the substrate coating results in tenfold reduction in hydrate adhesion strength independent of the thermal condition at which the hydrates form. Small variations in the measured strength of hydrate adhesion formed at different cooling temperature or time might be due to changes in the hydrate number.[48] Despite using the same wt% THF in water for all the tests ($\chi_{THF} = 0.19$) some of the ice water cages might not be occupied with the guest molecule,

www.MaterialsViews.com

ADVANCED
MATERIALS
INTERFACES
www.advmatinterfaces.de

FULL PAPER

THF. Once the hydrates form and are deposited on the fluoro-polymer bilayer films, their adhesion strengths are comparable regardless of their formation condition.

2.5. Durability of Coatings

One of the major concerns for developing effective hydrate-phobic coatings is achieving the necessary durability that is required for industrial applications. The surface properties of most polymer coatings degrade after undergoing repeated cycles of ice and/or hydrate formation and detachment. To investigate the durability of the coatings, we characterized the mechanical, surface, and hydrate-phobic properties of the coatings after two cycles of THF hydrate formation and detachment. To this end, silicon substrates that were used for the formation of THF hydrates (using ≈19 wt% THF in water) were reused for another set of hydrate formation and adhesion strength measurements.

The hydrate adhesion strength on reused LFG-BL (10 nm) and LFG-BL (40 nm) silicon substrates were found to be 308 ± 125 and 145 ± 87 kPa, respectively, which are within the same range of values obtained on as-deposited coatings (320 ± 84 kPa for LFG-BL (10 nm) and 128 ± 100 kPa for LFG-BL (40 nm), respectively). Advancing and receding contact angles of THF water droplets with $\chi_{THF} = 0.19$ were also remeasured after one hydrate adhesion/de-adhesion cycle on polymer coatings. The measured values were again within the same range of those obtained from measurements on as-deposited samples, as shown in **Table 3**. Measurements of the elastic modulus and hardness were also performed on the as-deposited coatings, and, after one cycle of hydrate adhesion tests and comparable values were obtained (see the Experimental Section).

In addition, scanning electron microscopy with energy dispersive X-ray spectrometer, SEM-EDS (JEOL 6010LA) was applied to verify the wettability and mechanical property results. A "+" crossmark was intentionally created on the sample prior to SEM-EDS to ensure EDS mapping with minimal drift in images, which can happen due to possible charge accumulation. SEM-EDS image and maps of distribution of elements on as-deposited coatings and after one hydrate adhesion/de-adhesion cycle indicates that the film is uniformly rich in fluorine and carbon over large areas (Figure S6, Supporting Information). These data indicate that the coatings developed in this study remain functional even after a freezing/THF hydrate deposition and de-adhesion cycle. In future tests, the performance of these iCVD polymer coatings will be studied under extended cycles of water immiscible hydrate formation and detachment and their durability evaluated after long-term contact with aqueous media and atmospheres with high humidity.[49,50]

2.6. Substrate Effect

A linker-free grafted bilayer pDVB/pPFDA with pPFDA thickness of 10 and 40 nm (which we denote as LFG-BL (10 nm) on steel and LFG-BL (40 nm) on steel, respectively) were also deposited on a rough steel substrate and their surface properties were again examined with optical profilometry (Table S2, Supporting Information). A RMS roughness value of $R_q = 112.2 \pm 7.5$ nm and $R_q = 119.5 \pm 7.7$ nm were obtained from measurement performed on the LFG-BL (10 nm) on steel and the LFG-BL (40 nm) on steel, respectively. The increase in the RMS roughness value of this polymer film when deposited on steel (as compared to the value measured on the silicon wafer) comes from the roughness of the underlying steel substrate.

Goniometric measurements of the ≈19 wt% THF in water ($\chi_{THF} = 0.19$) contact angles were performed on polymer-coated steel substrates with advancing and receding contact angles of ($\theta_A^{19wt\% THF in water} = 116.2° \pm 3.3°$ and $\theta_R^{19wt\% THF in water} = 103.2° \pm 5.3°$ on LFG-BL (10 nm)). Corresponding contact angle values measured on LFG-BL (40 nm) deposited on steel substrates were higher than those obtained on LFG-BL (10 nm) on steel ($\theta_A^{19wt\% THF in water} = 120.3° \pm 2.7°$ and $\theta_A^{19wt\% THF in water} = 112.2° \pm 3.5°$ on LFG-BL (40 nm) on steel). This slight increase in the values of the contact angles can similarly be explained to be due to the slightly higher fluorine concentration in the thicker film (40 nm) when compared to thinner film (10 nm) and/or differences in the crystallinity of the two coatings.[13,15] In addition, the higher contact angle values measured on coatings deposited on steel substrates when compared to the same coatings deposited on silicon substrates is due to the enhanced surface roughness of the bilayer film that is deposited on the steel (which originates from the rough steel substrate; Table S1, Supporting Information).[51]

Table 3. Mechanical, surface, and hydrate-phobic properties of the linker-free grafted bilayer pDVB/PPFDA with an ≈10 nm pPFDA (LFG-BL (10 nm)) and linker-free grafted bilayer pDVB/PPFDA with an ≈40 nm pPFDA (LFG-BL (40 nm)) coated silicon substrates were characterized on as-deposited coatings and after a complete hydrate adhesion test (hydrate formation and detachment). These data indicate that developed hydrate-phobic coatings are durable.

	As-deposited		After hydrate adhesion test	
	LFG-BL (10 nm)	LFG-BL (40 nm)	LFG-BL (10 nm)	LFC-BL (40 nm)
$\theta_A^{19 wt\% THF in water}$ [°]	110 ± 3.5	113.7 ± 4.5	102 ± 9.3	107 ± 8.7
$\theta_R^{19 wt\% THF in water}$ [°]	97 ± 4.0	110 ± 5.5	93 ± 7.3	99.2 ± 7.5
Hydrate adhesion strength [kPa]	320 ± 84	128 ± 100	308 ± 125	145 ± 87
Elastic modulus [GPa]	$18.1 \pm l.0$	19.1 ± 1.2	17.0 ± 1.4	16.6 ± 2.0
Hardness [MPa]	463 ± 4.5	479 ± 7.0	442 ± 5.0	440 ± 12.1

FULL PAPER

THF hydrates formed on bare and bilayer polymer-coated steel substrates from ≈19 wt% THF dissolved in water ($\chi_{THF} = 0.19$) under conditions similar to those explained earlier (2 h cooling at −15 °C) and the strength of THF hydrates adhesion was measured. The strength of the THF hydrate adhesion measured on bare steel substrates was 1130 ± 185 kPa, whereas the corresponding value on the thin (10 nm) and the thick (40 nm) bilayer films deposited on the rough steel substrates were measured to be 280 ± 95 and 153 ± 86 kPa, respectively. Similar to the bilayer coatings deposited on the silicon substrates, close to a tenfold decrease in the average strength of THF hydrate adhesion was observed when steel substrates were coated with these coatings. This reaffirms the effectiveness of these conformal bilayer coatings on substrates that are more representative of materials which would be found on the inside of an oil and gas pipeline.

3. Conclusion

In conclusion, substrates coated with bilayer polymer films consisting of a high crosslink density network topped with a 40 nm layer of fluorine rich polymer showed up to tenfold reduction in the average strength of hydrate adhesion. Experimental measurements of adhesion strength of ice/hydrate mixtures were well correlated using a relationship based on the adhesion strength of pure ice and pure hydrate. Thus, by measuring only the latter two pure component values, the adhesion value for any arbitrary mixture can be predicted. The measured adhesion strengths of ice, hydrate, and ice/hydrate mixtures were found to correlate well with the work of adhesion between liquid droplets used in their formation (either water or THF–water mixture) and underlying substrate. We showed that a solution with a composition of 19 wt% THF in water has to be used as a probe liquid for the evaluation of the adhesion strength of THF hydrates. The subcooling temperature and time of exposure were found to have no statistically significant impact on the adhesion strength of THF hydrates. This indicates that once the THF hydrates are formed and deposited on the surfaces, their adhesion strengths are comparable regardless of their formation condition. The coatings we have developed remain robustly hydrate-phobic after one cycle of formation and detachment of THF hydrates and have future potential for coating the inside of oil and gas pipelines for deep-sea operations. Future studies should include the formation and adhesion of water-immiscible hydrates (e.g., natural gas hydrates), in which hydrate formation is governed by water/guest surface area and interfacial thermal and mass transfer resistances.

4. Experimental Section

iCVD Coatings: In situ grafting and iCVD polymerizations were carried out in a custom-built cylindrical reactor (diameter 24.6 cm and height 3.8 cm), supporting an array of 14 parallel chromoalloy filaments (Goodfellow) suspended 2 cm from the stage.[13,15] The reactor was covered with a quartz top (2.5 cm thick) that allows real-time thickness monitoring by reflecting a 633 nm He–Ne laser source (JDS Uniphase) off the substrate/polymer and recording the interference signal intensity as a function of time. The reactor was pumped down by a mechanical

Fomblin pump (Leybold, Trivac) and the pressure was monitored with a MKS capacitive gauge. The liquid monomers (1H, 1H, 2H, 2H-perfluorodecyl acrylate, PFDA, 97% Aldrich) and (DVB, 80% Aldrich) and the initiator (TBPO, 98% Aldrich) were used as received without further purification. TBPO was kept at room temperature (T_f = 25 °C) and was delivered into the reactor through a mass flow controller (1479 MFC, MKS Instruments) at a constant flow rate of 3 sccm during grafting, and 3 and 1 sccm in DVB and PFDA during polymerization, respectively. Methyl radicals were formed through heating the filaments at T_f = 310 °C during grafting using a DC power supply (Sorensen), whereas initiator radicals (TBO) were created by breaking only the labile peroxide bond of the TBPO at filament temperature of T_f = 250 °C during polymerization. PFDA and DVB were vaporized in glass jars that were heated to 80 and 60 °C, respectively, and then introduced to the reactor through needle valves at constant flow rates of 0.1 and 1 sccm, respectively. The substrate temperature was kept at T_s = 20 °C during grafting and 30 °C during polymerization (within ± 1 °C) using a recirculating chiller/heater (NESLAB RTE-7). All of the temperatures were measured by K-type thermocouples (Omega Engineering). The working pressure was maintained at 800 mTorr during grafting and 650 and 300 mTorr in DVB and PFDA polymerization, respectively, using a throttle valve (MKS Instruments). Prior to in situ grafting, silicon wafers (Wafer World, Inc.) were first cleaned by sonication in acetone and isopropanol each for 5 min, followed by rinsing in DI water (>16 MΩ cm). The surfaces were then treated with oxygen plasma for 10 min for further cleaning and for creating surface hydroxyl groups prior to transfer into iCVD reactor.

THF–Water Surface Tension and Contact Angle Measurements: Surface tension of THF–water and contact angles were measured using a goniometer equipped with an automated dispenser (Model 500, ramé-hart). The surface tensions of THF–water mixtures were obtained through pendant drop method.[37] Measurements were performed rapidly to minimize impact of air exposure on THF–water droplets. The surface tension values were averaged from measurements of ten droplets for a given wt% of THF in water. Advancing and receding contact angles were measured with the sessile drop method by depositing a THF–water droplet of 2–3 µL on the surface, then increasing the volume by 0.15 µL increments until advancement in the liquid meniscus was observed and then decreasing by the same rate until receding motion was seen. Advancing contact angles were considered as the maximum angles observed during the droplet growth, while receding contact angles were measured in correspondence of the drop profile just before the interface receded. Each contact angle value was averaged from measurements of ten droplets of a given THF–water mixture distributed across the sample.

Strength of Ice/Hydrate Adhesion Measurements: The strength of crystal solids (ice and/or hydrate) adhesion was measured using a custom-built ice adhesion setup whose details are described elsewhere.[46,52] The samples were cut into 1.5 × 1.5 cm pieces and clamped to a base plate. Then, glass cuvettes with a 1 × 1 cm cross section ≈90% filled with THF–water mixture (0, 10, 19, 50, and 70 wt% THF in water) were inverted on them and clamped. Care was taken to remove any possible liquid residue on the substrate around the cuvettes. The entire plate was cooled at a rate of 2 °C s^{-1} to desired temperature on a Peltier plate (TECA Corporation, model LHP-800CP) in a low-humidity nitrogen atmosphere (humidity < 5%) and was maintained at this temperature for at desired time to ensure formation of crystal solids (ice and/or hydrates) within the cuvettes. The probe of a force transducer (Imada, model ZP-44) was used to apply a shear force to the cuvettes, and the maximum force required to fracture the crystal solid–substrate interface was recorded. The probe was located about 1.3 mm above the substrate surface to minimize torque on the ice sample. This distance was maintained the same for all samples with the same substrate type. The force measurement tests were performed on 20 samples of each type to minimize statistical variations. The maximum measured forces at the crystal solid–substrate break point were converted to a measure of the shear strength of solid (ice and/or hydrate) adhesion by dividing over the known cross-section area of the ice–substrate interface (1 cm^2).

Elastic Modulus and Hardness Measurements: A Nanovea mechanical tester (M1 P-Nano/AFM) was used during the nanoindentation test to obtain elastic modulus and hardness of the polymer coatings. The indenter-microscope calibration was performed using a copper sample with a maximum load of 20 mN and indenter approach speed of 30 μm min^{-1}. Depth and compliance calibration was performed on a fused silica sample with a Young's modulus of 72 GPa and Poisson's ratio of 0.17. A conical diamond indenter tip (Young's modulus = 1140 GPa and Poisson's ratio = 0.07) with a radius of R = 10 μm was used during all indentations. All of the polymer films used in the nanoindentation experiments were more than 1 μm thick. This was achieved by increasing the thickness of pDVB, while keeping the pPFDA thickness in the same range (10 or 40 nm thick). A maximum indentation depth of 25–150 nm was used to eliminate the possibility of substrate effects which complicate the subsequent analysis. In addition, exploratory tests were performed to ensure that the normal load did not experience a sudden change by a slight increase in the maximum penetration depth indicating that any underlying substrate effect was very minimal. A 4 × 4 grid was used during the indentation of the polymers, with 10 μm separation in both directions between indentations. The ASTM E2546 (ISO 14577) procedure was used by the software to obtain elastic modulus and hardness of the polymers for 16 indentations per sample. Maximum load, load rate, and the creep time were changed to evaluate the time response to loading of the polymers. Finally, a maximum load of 0.40 mN with 0.8 mN min^{-1} rate and creep time of 5 s were applied throughout the indentation measurements.[17] This ensured appropriate deformation of the polymer networks during loading/unloading cycles and enabled a linear fit to the load-penetration curves during unloading. The Poisson's ratio for all of the polymers was assumed to be the same and equal to 0.5.[53] A contact load of 0.05 mN was used during the nanoindentation measurements and the recording of the data were stopped once the normal load reached the contact load.

SEM-EDS Imaging: Polymer-coated substrates were sputter-coated with 5 nm of gold (Denton Desk V), and images were obtained by SEM (JEOL 6010LA) with an acceleration voltage of 15 kV. A high acceleration voltage was used to allow mapping without charge accumulation and drift of the images during the mapping. The black and white SEM image is intentionally out of clear focus to optimize the EDS analysis. The black and white images are computer-colored with assigned color schemes for specific elements. These images acquired on as-deposited coatings and after one cycle of hydrate formation, adhesion, and de-adhesion.

XPS Measurements: X-ray data were acquired using a spectrophotometer (PHI 5000*VersaProbe* II) with an Al Kα X-ray source. The survey scan spectra were collected at BE of 0–1100 eV with a step size of 0.8 eV, a pass energy of 187.8 eV, a TOA of 45°, and a spot size of 200 μm. Figure S2a, Supporting Information, shows survey scan spectra randomly collected from LFG-BL (10 nm) and LFG-BL (40 nm) on silicon substrate. The scan showed the most prominent peaks to be C1s, O1s, and F1s. The appearance of an F1s peak centered at 688.4 eV confirms the presence of fluorine groups on the bilayer film. High resolution XPS spectra of F1s and C1s binding energy were also acquired over binding energy of 680–700 and 279–299 eV, respectively (Figure S2b,c, Supporting Information). For high resolution, the instrument was utilized in a high power mode with a raster scan of 100 μm spot over a line of 1.4 mm long. The pass energy and step size for high resolution spectra were 23.5 and 0.1 eV, respectively. Each measurement was examined in several spots to ensure reproducibility. Multipack software was utilized for analysis of the collected spectra, where 70% Gaussian-30% Lorentzian curve fitting was performed. The C1s XPS spectrum can be described using the five bonding environments expected due to vinyl polymerization of the PFDA monomer. Table S1, Supporting Information, shows the position of each peak and its comparison to the theoretical values.

Supporting Information

Supporting Information is available from the Wiley Online Library or from the author.

[1] P. T. Beurskens, G. A. Jeffrey, *J. Chem. Phys.* **1964**, *40*, 906.

[2] S. Gao, *Energy Fuels* **2008**, *22*, 3150.

[3] Y. A. Dyadin, I. V. Bondaryuk, L. S. Aladko, *J. Struct. Chem.* **1995**, *36*, 995.

[4] P. Bollavaram, S. Devarakonda, M. S. Selim, E. D. Sloan, *Annals of the New York Academy of Sciences*, Gas Hydrates: Challenges for the Future, (Eds: G. D. Holder, P. R. Bishnoi), **2000**, p. 533, Vol. *912*.

[5] P. W. Wilson, D. Lester, A. D. J. Haymet, *Chem. Eng. Sci.* **2005**, *60*, 2937.

[6] A. F. Heneghan, P. W. Wilson, G. M. Wang, A. D. J. Haymet, *J. Chem. Phys.* **2001**, *115*, 7599.

[7] A. K. Sum, C. A. Koh, E. D. Sloan, *Ind. Eng. Chem. Res.* **2009**, *48*, 7457.

[8] B. C. Gbaruko, J. C. Igwe, P. N. Gbaruko, R. C. Nwokeoma, *J. Pet. Sci. Eng.* **2007**, *56*, 192.

[9] S. Devarakonda, A. Groysman, A. S. Myerson, *J. Cryst. Growth* **1999**, *204*, 525.

[10] C. A. Koh, R. E. Westacott, W. Zhang, K. Hirachand, J. L. Creek, A. K. Soper, *Fluid Phase Equilib.* **2002**, *194*, 143.

[11] J. D. Smith, A. J. Meuler, H. L. Bralower, R. Venkatesan, S. Subramanian, R. E. Cohen, G. H. McKinley, K. K. Varanasi, *Phys. Chem. Chem. Phys.* **2012**, *14*, 6013.

[12] A. M. Coclite, R. M. Howden, D. C. Borrelli, C. D. Petruczok, R. Yang, J. L. Yague, A. Ugur, N. Chen, S. Lee, W. J. Jo, A. D. Liu, X. X. Wang, K. K. Gleason, *Adv. Mater.* **2013**, *25*, 5392.

[13] A. M. Coclite, Y. J. Shi, K. K. Gleason, *Adv. Mater.* **2012**, *24*, 4534.

[14] G. Ozaydin-Ince, A. M. Coclite, K. K. Gleason, *Rep. Prog. Phys.* **2012**, *75*, 016501.

[15] A. M. Coclite, Y. J. Shi, K. K. Gleason, *Adv. Funct. Mater.* **2012**, *22*, 2167.

[16] J. L. Yague, K. K. Gleason, *Macromolecules* **2013**, *46*, 6548.

[17] H. Sojoudi, G. H. McKinley, K. K. Gleason, *Mater. Horizons* **2015**, *2*, 91.

[18] S. Technology, Vol. 2014, **2014**.

[19] Y. Sabase, K. Nagashima, *J. Phys. Chem. B* **2009**, *113*, 15304.

[20] K. L. Pinder, *Can. J. Chem. Eng.* **1965**, *43*, 271.

[21] S. R. Gough, D. W. Davidson, *Can. J. Chem.* **1971**, *49*, 2691.

[22] T. Iida, H. Mori, T. Mochizuki, Y. H. Mori, *Chem. Eng. Sci.* **2001**, *56*, 4747.

[23] H. Pahlavanzadeh, A. Kamran-Pirzaman, A. H. Mohammadi, *Fluid Phase Equilib.* **2012**, *320*, 32.

[24] R. Signer, H. Arm, H. Daeniker, *Helv. Chim. Acta* **1969**, *52*, 2347.

[25] R. Ohmura, T. Shigetomi, Y. H. Mori, *J. Cryst. Growth* **1999**, *196*, 164.

[26] C. J. Taylor, L. E. Dieker, K. T. Miller, C. A. Koh, E. D. Sloan, *J. Colloid Interface Sci.* **2007**, *306*, 255.

[27] L. E. Dieker, Z. M. Aman, N. C. George, A. K. Sum, E. D. Sloan, C. A. Koh, *Energy Fuels* **2009**, *23*, 5966.

[28] S. O. Yang, D. M. Kleehammer, Z. X. Huo, E. D. Sloan, K. T. Miller, *J. Colloid Interface Sci.* **2004**, *277*, 335.

[29] Z. M. Aman, E. P. Brown, E. D. Sloan, A. K. Sum, C. A. Koh, *Phys. Chem. Chem. Phys.* **2011**, *13*, 19796.

[30] G. Aspenes, L. E. Dieker, Z. M. Aman, S. Hoiland, A. K. Sum, C. A. Koh, E. D. Sloan, *J. Colloid Interface Sci.* **2010**, *343*, 529.

[31] J. H. Song, A. Couzis, J. W. Lee, *Langmuir* **2010**, *26*, 9187.

ADVANCED
MATERIALS
INTERFACES

www.advmatinterfaces.de

Materials
Views

www.MaterialsViews.com

FULL PAPER

[32] J. H. Song, A. Couzis, J. W. Lee, *Langmuir* **2010**, *26*, 18119.

[33] G. Ozaydin-Ince, K. K. Gleason, *J. Vac. Sci. Technol. A* **2009**, *27*, 1135.

[34] R. Yang, T. Buonassisi, K. K. Gleason, *Adv. Mater.* **2013**, *25*, 2078.

[35] C. D. Petruczok, R. Yang, K. K. Gleason, *Macromolecules* **2013**, *46*, 1832.

[36] D. D. Purkayastha, V. Madhurima, *J. Mol. Liq.* **2013**, *187*, 54.

[37] G. W. Smith, L. V. Sorg, *J. Phys. Chem.* **1941**, *45*, 671.

[38] J. Drelich, K. L. Mittal, J. S. Laskowski, *Apparent and Microscopic Contact Angles*, Taylor and Francis, London, **2000**.

[39] E. J. De Souza, L. C. Gao, T. J. McCarthy, E. Arzt, A. J. Crosby, *Langmuir* **2008**, *24*, 1391.

[40] L. C. Gao, T. J. McCarthy, *Langmuir* **2008**, *24*, 9183.

[41] L. C. Gao, T. J. McCarthy, *Langmuir* **2009**, *25*, 14105.

[42] V. Kumar, J. Pulpytel, F. Arefi-Khonsari, *Plasma Process. Polym.* **2010**, *7*, 939.

[43] G. Beasmon, D. Briggs, *High resolution XPS of organic polymers—the scienta ESCA 300 data base*, Wiley, Chichester, **1992**.

[44] M. Gupta, K. K. Gleason, *Langmuir* **2006**, *22*, 10047.

[45] M. Muro, M. Harada, T. Hasegawa, T. Okada, *J. Phys. Chem. C* **2012**, *116*, 13296.

[46] A. J. Meuler, J. D. Smith, K. K. Varanasi, J. M. Mabry, G. H. McKinley, R. E. Cohen, *ACS Appl. Mater. Interfaces* **2010**, *2*, 3100.

[47] P. Kim, T. S. Wong, J. Alvarenga, M. J. Kreder, W. E. Adorno-Martinez, J. Aizenberg, *ACS Nano* **2012**, *6*, 6569.

[48] D. Corak, T. Barth, S. Hoiland, T. Skodvin, R. Larsen, T. Skjetne, *Desalination* **2011**, *278*, 268.

[49] R. Menini, Z. Ghalmi, M. Farzaneh, *Cold Reg. Sci. Technol.* **2011**, *65*, 65.

[50] L. B. Boinovich, A. M. Emelyanenko, V. K. Ivanov, A. S. Pashinin, *ACS Appl. Mater. Interfaces* **2013**, *5*, 2549.

[51] A. Hennig, K. Grundke, R. Frenzel, M. Stamm, *Tenside Surf. Deter.* **2002**, *39*, 243.

[52] S. B. Subramanyam, K. Rykaczewski, K. K. Varanasi, *Langmuir* **2013**, *29*, 13414.

[53] J. J. Xu, A. Asatekin, K. K. Gleason, *Adv. Mater.* **2012**, *24*, 3692.